Shen, J.; Lifante, J.; Fernández, N.; Jaque, D.; Ximendes, E.; *ACS Nano* 2020. doi: 10.1021/acsnano.9b08824

In Vivo Spectral Distortions of Infrared Luminescent Nanothermometers Compromise Their Reliability

Yingli Shen[1], José Lifante[1,2], Nuria Fernández[2,3], Erving Ximendes[1,3]*, Daniel Jaque[1,3]

[1] Fluorescence Imaging Group, Departamento de Física de Materiales – Facultad de Ciencias, Universidad Autónoma de Madrid, C/Francisco Tomás y Valiente 7, Madrid 28049, Spain

[2] Fluorescence Imaging Group, Departamento de Fisiología – Facultad de Medicina, Avda. Arzobispo Morcillo 2, Universidad Autónoma de Madrid, Madrid 28029, Spain

[3] Nanobiology Group, Instituto Ramón y Cajal de Investigación Sanitaria, IRYCIS, Ctra. Colmenar km. 9.100, Madrid 28034, Spain

E-mail: erving.ximendes@inv.uam.es

Abstract

Luminescence nanothermometry has emerged over the last decade as an exciting field of research due to its potential applications where conventional methods have demonstrated to be ineffective. Preclinical research has been one of the areas that have benefited the most from the innovations proposed in the field. Luminescent nanothermometers have starred unimaginable advances such as *in vivo* intratumoral thermal reading or brain activity monitoring through real-time thermal sensing. Nevertheless, certain questions concerning the reliability of the technique under *in vivo* conditions have been continuously neglected by most of the scientific community. In this work, hyperspectral *in vivo* imaging demonstrates that *in vivo* luminescent nanothermometry is not as reliable as previously thought. This work, indeed, reveals how the temperature-dependent optical transmittance of living tissues can induce spectral changes in the measured fluorescence. These changes, in turns, can be wrongly attributed to temperature variations. The next steps that should be taken in the future for a reliable *in vivo* luminescence nanothermometry are discussed together with a perspective view of the field after the findings that are here reported.

INTRODUCTION

Minimally invasive high-resolution *in vivo* thermal sensing is highly desired by biomedical researchers working in preclinical applications. Among the different reasons that drew the attention of the scientific community to this specific application was the fact that contactless thermometry could be used as a tool for the early diagnosis of several diseases as well as for improving the efficacy of thermal therapies.[1–5] As a consequence, there has been a fast development of what is now called luminescence nanothermometry (LNTh). LNTh is based on the use of luminescent nanoparticles (LNPs) whose spectroscopic properties are thermally dependent in the physiological range of temperature (10–50 °C).[6–20] Different fluorescent compounds, including organic dyes, fluorescent proteins and a large variety of NPs (metallic, dielectric doped with rare-earth ions, quantum dots, etc.), have already been successfully used for *in vivo* remote thermal sensing.[21–23] When compared to other thermometry methods, LNTh presents the advantage of being minimally invasive, cost-effective and experimentally simple.

Although LNTh is in its early stages, a good number of preclinical applications have already been demonstrated thanks to the appearance of luminescent nanothermometers working in the spectral ranges known as biological windows (BWs),[24–34] where absorption and scattering of light in biological tissues are minimized.[35–42] Luminescent nanothermometers working in the infrared biological windows have made possible: deep abdominal temperature sensing,[43] *in vivo* recording of subcutaneous thermal videos,[44,45] and the identification of incipient diseases (such as ischemia or the presence of tumors).[46–48] Thereupon, the scientific community became aware of the necessity to enhance the properties (such as brightness or thermal sensitivity) of the available luminescent thermometers. Nevertheless, certain questions concerning their reliability are now arising.[49] It has been reported, for instance, that some artefacts may arise from system inhomogeneities,[50] from the limitations of the detection system,[51] from the interference of contaminants or external signals,[52] and/or from an unexpected dependence of the system's response under the experimental conditions.[53,54] The partial self-absorption (SA) of luminescence (i.e. when there is an overlap between the excitation and emission spectra), additionally, could be a factor that alters the spectral shape of rare-earth-based LNThs and, to some degree, of dyes and QDs.[49]

However, there is an artefact that remains overlooked by the scientific community. In general, it is simply assumed that if one designs a luminescent nanothermometer that operates in the BWs, then the interplay between tissue-induced attenuation and the luminescence that carries the thermal information can, in a good approximation, be neglected. This assumption implies that the collected luminescence has the same spectral properties of the luminescence generated by the deep-tissue allocated nanothermometers. Though the low attenuation coefficient of tissues in the BWs assures a maximized penetration depth of light, it does not warrantee the lack of spectral distortions. In fact, under most *in vivo* experimental conditions, the wavelength dependence of the optical properties of a tissue could give rise to such distortions.[55–59] They, in turns, could yield valuable information, for instance, on the oxygenation state and structure of a tissue.[60,61]

LNTh depends on the experimental determination of spectroscopic parameters such as (i) luminescence intensity, (ii) luminescence intensity ratio (LIR), (iii) spectral bandwidth, and (iv) wavelength position of an emission line.[6] Therefore, it is reasonable to think that the thermal readouts obtained with this technique could be affected by the tissue-induced distortions of spectra. Yet, when retrieving the literature, it is not possible to find any work connecting those two concepts. This could be mostly attributed to the lack of spectral resolution in the majority of infrared imaging equipment utilized for *in vivo* fluorescence imaging experiments. Indeed, the detection of *in vivo* tissue-induced spectral distortions is not an easy task at all. Recently, however, Hyperspectral Imaging (HSI) has been presenting itself as an automated spectrally sensitive technology that integrates imaging and conventional spectroscopy in such a way that it provides complementary information from both domains.[62–67] This technology, therefore, could, in principle, be easily applied to gather information on attenuation-induced spectra distortions.

In this work, *in vivo* HSI is used to experimentally evaluate the magnitude of the tissue-induced spectral distortions in the luminescence of acclaimed nanothermometers. The origin of these distortions is discussed in terms of the optical properties of several tissues. The implications that they have on *in vivo* LNTh are discussed in detail. Moreover, the next steps that should be taken in future studies are also discussed.

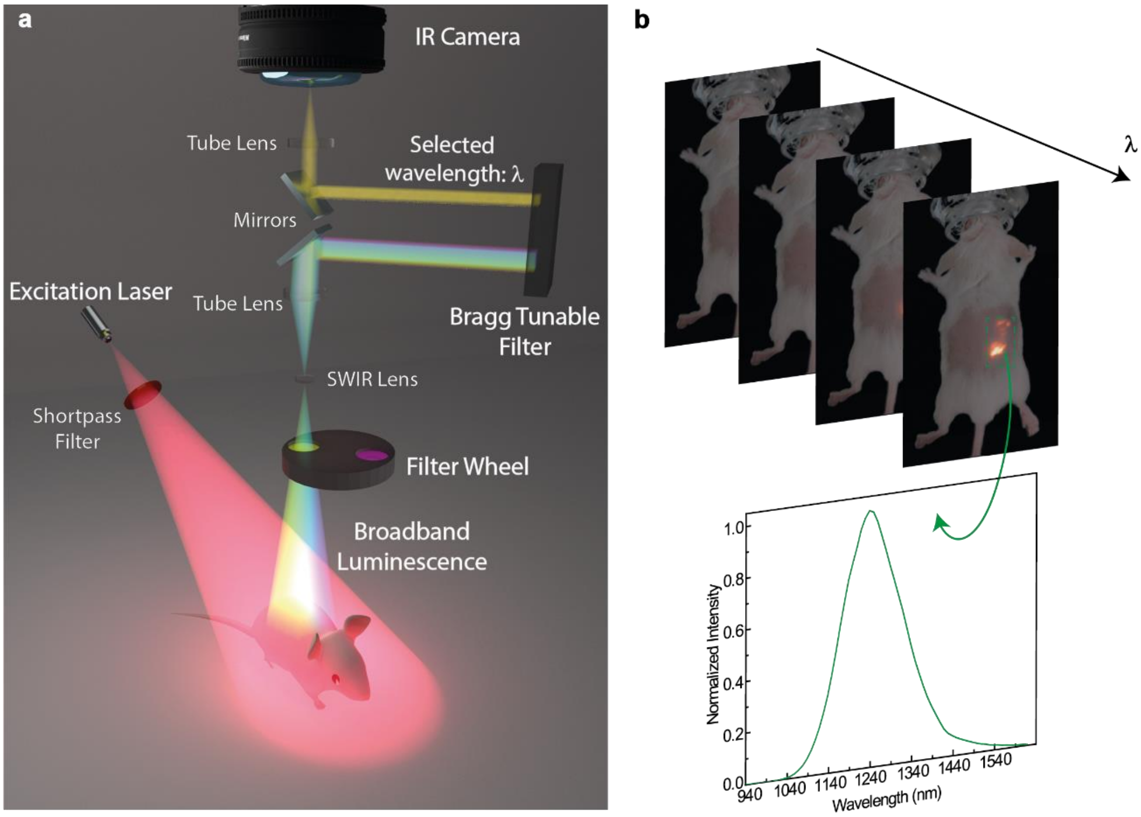

Figure 1. Hyperspectral Imaging. a) Schematic representation of the hyperspectral imaging system used in this work. **b)** Representative stack of narrow band sub-images of a mouse injected with Ag_2S dots. The images form a 3D hypercube from which one obtains the emission spectrum corresponding to a selected region.

Figure 1a shows a schematic diagram of the HSI system used in this work for the acquisition of luminescence spectra generated by nanothermometers. Briefly speaking, the optical excitation of the samples under study was provided by a fiber-coupled laser diode. A short-pass filter was used to block the long-wavelength tail of the laser source. The scattered light emitted from the sample was transmitted through a long-pass filter (Thorlabs FL0850, put in a filter wheel) that was intended to suppress the laser signal. Tube and shortwave Infrared (SWIR) lenses were then used as a relay to image the pupil on a Bragg Tunable Filter (BTF) which, in turns, would select a specific wavelength, λ, of the coming light.[55] This filtered light was then focused, by a second tube lens, on an infrared camera (ZephIRTM 1.7) to produce a monochromatic image. Synchronous tuning of the BTF and image acquisition allowed the obtainment of monochromatic fluorescence images corresponding to different emission wavelengths ranging from 900 up to 1700 nm. Under those circumstances, a 3D spatial map of spectral variation, *i.e.* a HSI cube, was built: the first two dimensions provided spatial information and a third dimension accounted for the spectral information.[56–58,68] The intensity values of a particular pixel in a HIS cube characterized its unique spectral fingerprint. As an example, the HSI cube of a colloidal solution of Ag_2S dots is shown in **Figure 1b,** from which their emission spectrum is obtained.

RESULTS AND DISCUSSION

Tissue-induced spectral distortions.

If an optically excited luminescent nanothermometer is under a tissue of thickness *L* then, according to the Modified Beer-Lambert Law, the luminescence intensity at wavelength λ detected ($I_{det}(\lambda)$) after passing through the tissue is given by:[69–72]

$$I_{det}(\lambda) = I_o(\lambda) e^{-g(\lambda) - L \times [\sum_i \epsilon_i(\lambda) \times DPF(\lambda)]} \qquad (1)$$

where $I_o(\lambda)$ is the actual luminescence intensity generated by the nanothermometers at wavelength λ, *g* is a function that accounts for the light intensity loss due to scattering, ε_i is the molar extinction coefficient of the i-th chromophore found in the tissue and *DPF* is the *Differential Pathlength Factor* (*i.e.* a parameter that accounts for increases in optical paths). Eq. 1 clearly states that $I_{det}(\lambda) \neq I_o(\lambda)$. In general, past works consider that the detected signal was proportional to the emitted signal for all the emission wavelengths (i.e. $I_{det}(\lambda) = k \cdot I_o(\lambda)$). This is to say that the extinction coefficients of a tissue are wavelength-independent, which is known to be false. Nevertheless, the impact of tissue absorption in the shape of the detected luminescence generated by nanothermometers remains uninvestigated. To work around this problem, a simple experiment with two CD1 mice was conceived. The first mouse was subjected to a subcutaneous injection of a Ag_2S dots while the second one was subjected to an intravenous injection of a solution of Ag_2S dots. More details can be found in the Experimental Section. **Figure 2a** and **2b** show the fluorescence images obtained in each case for an emission wavelength of 1200 nm. In the case of intravenous injection, the signal was generated by the Ag_2S dots accumulated in the liver. The luminescence spectra obtained from the HIS cubes obtained in each case are shown in **Figure 2d** and **2e.** While the subcutaneous injection provides a luminescence spectrum almost identical to the one generated by Ag_2S dots in colloidal solution (see **Figure 1**), the detected emission spectrum corresponding to the NPs accumulated in the liver differs by a great amount. In principle, this spectral distortion can be attributed to either the tissue absorption or to a modification of Ag_2S dots in the liver because, for instance, of pH change. To rule out this second possibility, the mouse subjected to intravenous injection was sacrificed in order to obtain the *ex vivo* fluorescence image and spectrum of the liver. Results are shown in **Figure 2c** and **2f**, respectively. As one can notice, there is an obvious similarity with the original spectrum of Ag_2S dots. This concludes that Ag_2S dots have not been significantly modified when accumulated in the liver and that the *in vivo* spectral distortion obeys the wavelength-dependent attenuation of tissues between the liver and the detection system (including vessels, skin, etc.). The data included in **Figure 2**, therefore, clearly state that tissue-induced spectral distortions cannot be neglected. Otherwise, the analysis of the *in vivo* spectra of optical probes can lead to false conclusions.

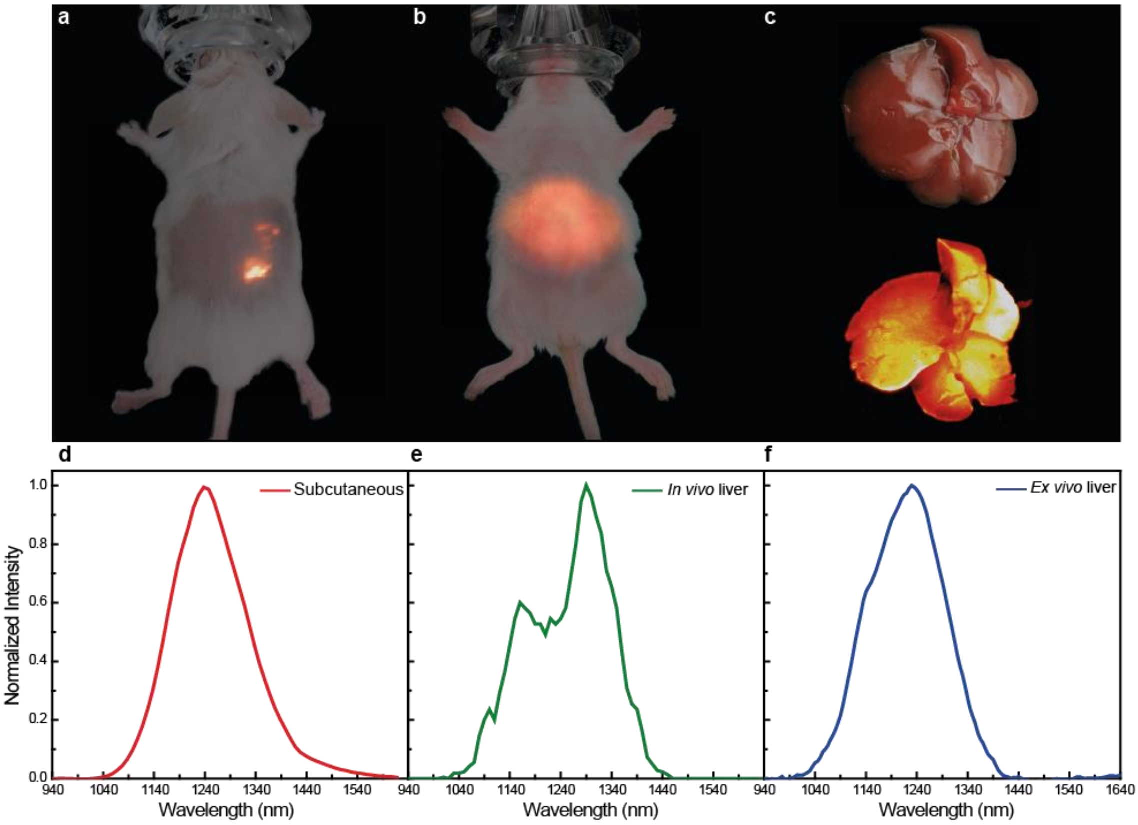

Figure 2. Spectral variations of Ag_2S dots under different conditions. Luminescence image generated by Ag_2S dots after **a)** a subcutaneous injection in a CD1 mouse, **b)** a retroorbital injection in a living mouse and **c)** sacrificing the mouse and isolating the liver (*ex-vivo* conditions). Emission spectra of **d)** subcutaneous injection, **e)** retroorbital injection and **f)** isolated liver after retroorbital injection. The optical images of mouse and liver were included (or superimposed) in **a**, **b** and **c** for a better visualization.

Tissue-induced spectral distortions are not restricted to the case of Ag_2S dots. The performance of other infrared luminescent nanothermometers is also expected to be affected. Though many have been proposed for *in vivo* thermal sensing, Yb@Nd LaF_3 and Er-Yb@Yb-Tm LaF_3 NPs were selected in this work as representative examples. They are, indeed, good systems to examine due to their good thermal sensitivity and broad ranges of emission inside the BWs.[44,45,73] **Figures 3a** and **3b** show the broadband infrared luminescence images (850-1600 nm) of a cuvette filled with an aqueous solution of Yb@Nd LaF_3 NPs and of a mouse subjected to an subcutaneous injection of the same NPs, respectively. **Figure 3c** shows the emission spectra obtained from the HSI cubes of the Yb@Nd LaF_3 NPs in a colloidal suspension and the Yb@Nd LaF_3 NPs subcutaneously allocated. The skin-induced distortions in the emission spectra are evident. Indeed, they affect the intensity ratio between emissions at 980 and 1060 nm which, in turns, is commonly used for thermal sensing. **Figure 3d** and **3e** show the broadband infrared luminescence images (850-1600 nm) of a cuvette filled with an aqueous solution of Er-Yb@Yb-Tm LaF_3 NPs and of a mouse subjected to an subcutaneous injection of the same NPs, respectively. In this case, the skin-induced spectral distortions are even more evident than those observed for Ag_2S and Yb@Nd LaF_3 NPs (see **Figure 3f**). In particular, skin absorption leads to a relevant reduction in the relative intensities of the emission bands centered at 1230 and 1470 nm, of Tm^{3+}, also used for ratiometric thermal sensing.

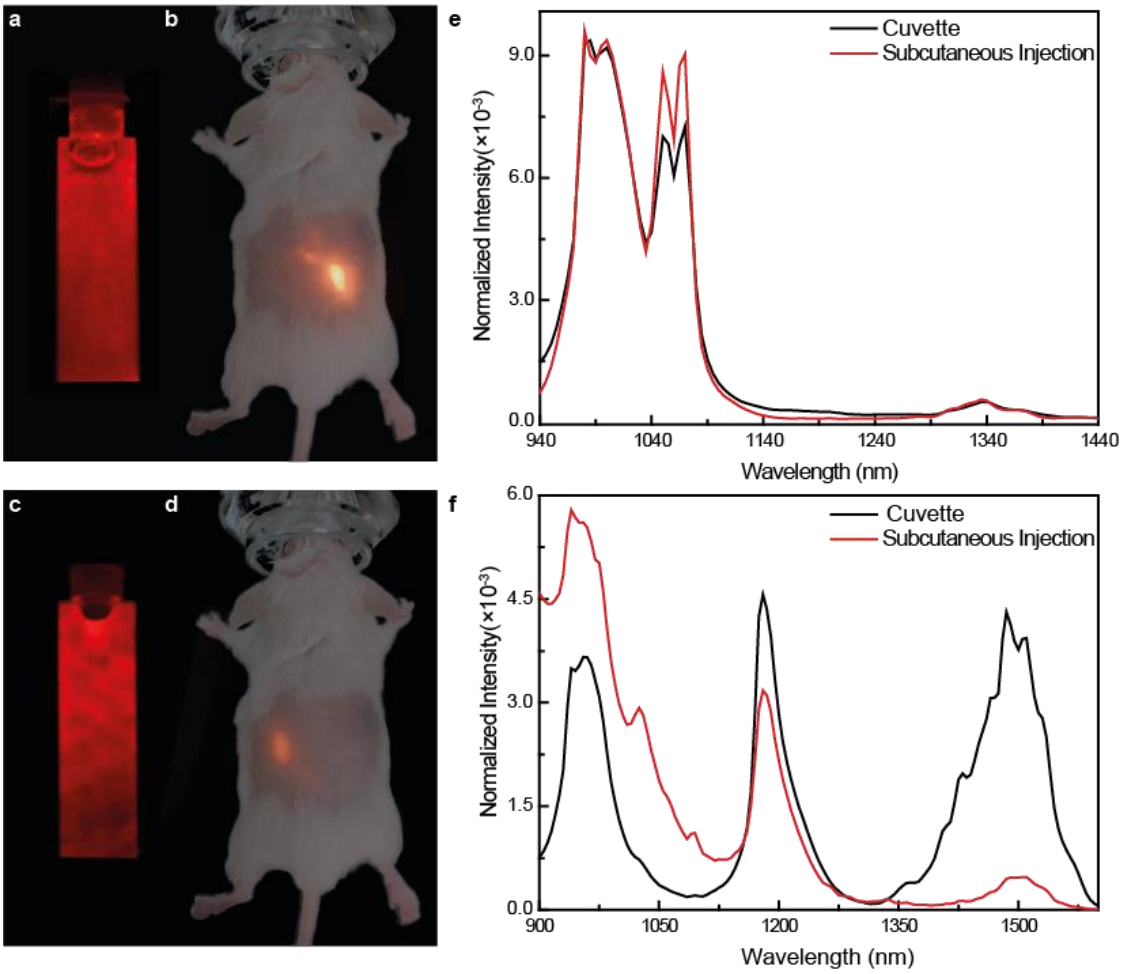

Figure 3. Luminescence of Yb@Nd LaF3 NPs and SWCNTs subcutaneous injections. Luminescence images of **a)** cuvette containing Yb@Nd LaF_3 NPs, **b)** subcutaneous injection of Yb@Nd LaF_3 NPs in a living mouse, **c)** cuvette containing Er-Yb@Yb-Tm LaF_3 NPs and **d)** subcutaneous injection of Er-Yb@Yb-Tm LaF_3 NPs in a living mouse. Emission spectra of the cuvette and subcutaneous injection corresponding to **e)** Yb@Nd LaF_3 NPs and **f)** Er-Yb@Yb-Tm LaF_3 NPs. The optical image of the mouse was superimposed in **b** and **d** for a better visualization.

Figures 2 and **3** clearly reveal how the optical attenuation caused by skin could lead to relevant spectral distortions in subcutaneously injected luminescent nanothermometers. But when dealing with other applications (such as brain thermometry), skin will not be the only organ contributing to the net spectral distortion. In fact, it is expected that distinct tissues would contribute differently due to their particular optical properties. In addition, depending on their emission spectra, different luminescent nanoparticles will suffer from distinct spectral distortions for a given tissue. In order to evaluate this, some *ex-vivo* experiments were conducted. Thin pieces of different tissues (taken from a group of sacrificed CD1 mice) were put on the surface of a cuvette containing solutions of either Ag_2S dots, Yb@Nd LaF_3 NPs or Er-Yb@Yb-Tm LaF_3 NPs. HSI cubes were then measured and the luminescence spectra as obtained in presence of different tissues were recorded. Figure S1 of Supporting Information contains some of the monochromatic HSI images taken throughout the experiment. Representative examples are included in **Figure 4a**, **b** and **c**. These figures include, for each type of NP, the emission spectra in absence of any tissue, in the presence of a 2 mm thick skin sample and in the presence of a 2 mm thick cortex tissue. In all the cases, the presence of the tissues lead to a significant spectral distortion. In order to quantify it, the percentual difference, σ, in the spectral shape with respect to the non-affected spectrum is defined as:

$$\sigma_{tissue} = \int |I_{tissue}^{norm}(\lambda) - I_{non-att}^{norm}(\lambda)| d\lambda \tag{2}$$

where the sup-index *norm* indicates that the spectrum was normalized to the area (i.e. $I_{norm}(\lambda) = I(\lambda)/\int I(\lambda)d\lambda$), I_{tissue} and $I_{non-att}$ stand for the spectra obtained with and without the tissue, respectively. The results are summarized in **Figure 4 d**, **e** and **f** where σ was analyzed for skin, muscle, skull, cortex, cerebellum and brainstem for Ag_2S dots, Yb@Nd LaF_3 NPs and Er-Yb@Yb-Tm LaF_3 NPs, respectively. As one can see, the variation on the shape of the spectra is more pronounced in some tissues than in others and it depends on the spectral regions that the luminescent nanothermometers emit. The transmitted luminescence of Er-Yb@Yb-Tm LaF_3, for instance, is the one which is mostly affected, due to the overlap of its emission with the water absorption peaks at 980 and 1500 nm. Another interesting aspect is that, depending on the wavelength range of operation of the luminescent thermometers, the combination of tissues in a multilayer structure can have opposite or agreeing contributions in the shape of the spectrum (as the *Skin+Muscle+Skull* structure demonstrates in **Figure 4 d**, **e** and **f**). The minimal measured value for the percentual difference was found to be close to 4% (skull in **Figure 4f**).

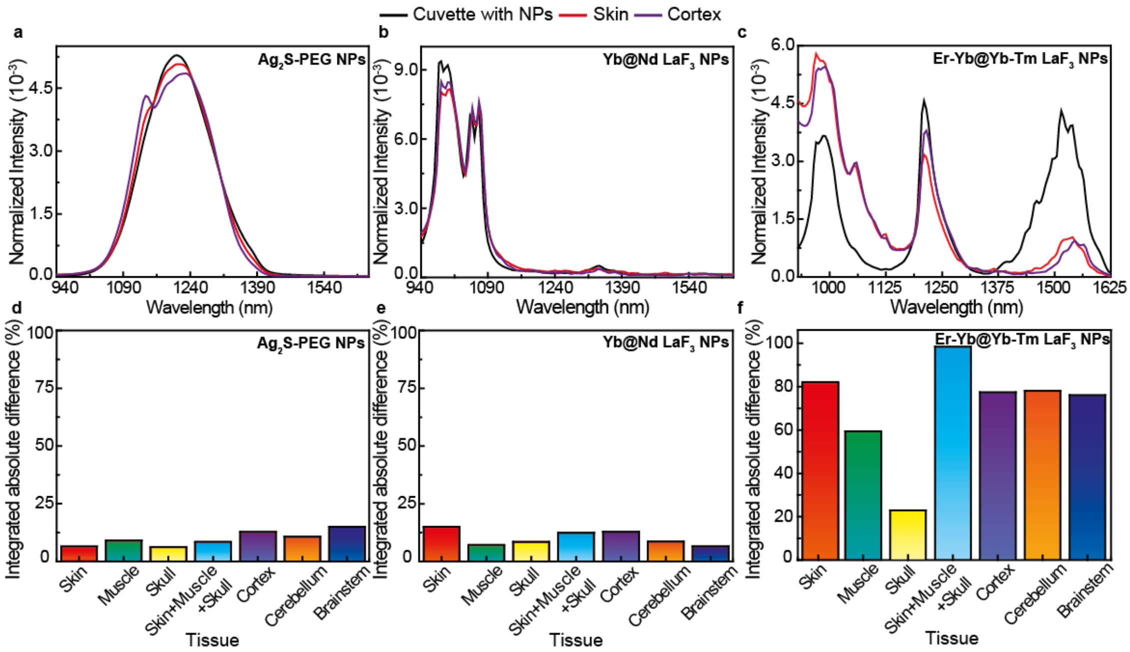

Figure 4. Tissue-induced changes in luminescence spectra of different NPs. Luminescence spectra of different cuvettes containing a solution of either **a)** Ag_2S NPs, **b)** Yb@Nd LaF_3 NPs or **c)** Er-Yb@Yb-Tm LaF_3 NPs when having no tissue (black), skin tissue (red) or brain cortex (purple) on their surfaces. Tissue-induced percentual difference of luminescence spectrum shape of **d)** Ag_2S NPs, **e)** Yb@Nd LaF_3 NPs and **f)** Er-Yb@Yb-Tm LaF_3 NPs.

Impact on *in vivo* thermometry.

Figure 4 reveals the serious limitations of luminescent nanothermometers to provide absolute temperature readouts. Despite its apparent insignificance, even small percentual differences in the emission spectra caused by tissue-induced distortions could lead to relevant deviations in the absolute thermal readout. In fact, depending on the selected thermometric parameter Δ, the error in the temperature estimation, δT, could be of the same order of magnitude as σ/S, where S is the relative thermal sensitivity of the thermometer (defined as $\frac{1}{\Delta}\left|\frac{d\Delta}{dT}\right|$). Given that most of luminescent thermometers that operate in the BWs present a relative thermal sensitivity of the order of $1\%\,^{o}C^{-1}$, a σ of 4% could lead to an error of $\pm 4\,^{o}C$ in the measurement of the absolute temperature. In worse scenarios, such as the case of Er-Yb@Yb-Tm LaF_3 NPs, this error could be magnified due to their higher values of σ.

A good number of recently proposed applications of luminescent nanothermometers mostly deals with measurements of temperature variations rather than absolute temperature determination. This is the case of *in vivo* thermal transient studies or thermal control during tumor ablation.[74,75] Nevertheless, several works have reported that the optical properties of tissues (specially its transmittance) could be temperature-dependent.[76–84] Consequently, tissue-induced distortions in the emission spectra of luminescent nanothermometers would also be a function of temperature. This, in turns, could compromise the use of LNTh for *in vivo* determination of temperature variations. According to expression (1), if the molar extinction coefficient of the chromophores present in the tissue are temperature-dependent (i.e. $\epsilon_i = \epsilon_i(\lambda, T)$), then the *in vivo* calibration curve of any given nanothermometer would not only be given by the temperature variation of the thermometric parameter ($\frac{d\Delta}{dT}$) but also by the temperature variation of the tissue optical properties. In order to evaluate the importance of this second term, it is necessary to compare the calibration curves in the presence and absence of a biological tissue. Given that Ag_2S dots present the possibility of using the ratio, intensity or peak position as thermometric parameters with relatively high thermal sensitivities, this particular luminescent thermometer was selected for the following set of experiments. A thin piece of tissue (2 mm) was put on the surface of a micro-chamber containing a solution of Ag_2S dots. The brainstem was chosen as the representative tissue due to its high induced percentual difference in the spectral shape of Ag_2S dots (**Figure 4d**). The temperature of the microchamber (with and without tissue) was varied (**Figure 5a**) and the corresponding emission spectra were measured. Experimental details concerning the calibration are found in the Experimental Section**.** Representative monochromatic luminescence images and emission spectra can be found in Section S2 of Supporting Information. By choosing a specific thermometric parameter Δ and using the standardized definition of the relative thermal sensitivity ($S_\Delta = \frac{1}{\Delta}\left|\frac{d\Delta}{dT}\right|$), the analysis of the emission spectra in the presence/absence of tissue (as obtained at different temperatures) allowed us to determine the variation of S_Δ. Clear differences are observed when using the emitted intensity at 1220 nm (*Int,* **Figure 5b**), the intensity ratio (*Ratio* = $Int_{1180nm}/Int_{1260nm}$, **Figure 5c**) or peak position (λ_{max}, **Figure 5d**) as thermometric parameters. The data suggest a general decrease in *S* due to the presence of brainstem (a pattern that is followed by other tissues, as seen in Figure S2 of Supporting Information). The greatest variation is found for S_{Int}, which provided an average decrease of 1.8 % $^{\circ}C^{-1}$. S_{Ratio} and $S_{\lambda_{max}}$, on the other hand, presented average decreases of 0.2 and 0.03 % $^{\circ}C^{-1}$, respectively.

As discussed in Section S3 of Supporting Information, the experimentally observed variations in S_Δ can be mainly attributed to the temperature-dependent optical properties of tissues. Thus, Equation (1) can be re-written as:

$$I(\lambda, T, L) = I_o(\lambda, T) e^{-L\,\mu_{att}^{eff}(\lambda, T, L)} \qquad (3)$$

where, for the sake of simplicity, $\mu_{att}^{eff}(\lambda, T, L) = [\sum_i \epsilon_i(\lambda, T) \times DPF\,(\lambda, T)] + g(\lambda, T)/L$ was defined as the effective attenuation coefficient. Under this form, it becomes easier to infer that the thermal dependence of μ_{att}^{eff} is the main reason for the observed changes in the value of *S.* As discussed in Section S4 of Supporting Information, when selecting different thermometric parameters, $\mu_{att}^{eff}(\lambda, T)$ will contribute in a different way. If we denote $S_{Int}^{att}(T)$ and $S_{Int}(T)$ as the thermal sensitivities relative to the emitted intensity at temperature T in the presence and absence of tissues, respectively, one could write:

$$\left|S_{Int}^{att}(T) - S_{Int}(T)\right| \le \left|L\frac{d\mu(\lambda_c,T,L)}{dT}\right|$$

At the same time, if we denote $S_{Ratio}^{t}(T)$ and $S_{Ratio}(T)$ as the thermal sensitivities relative to the intensity ratio at temperature T in the presence and absence of tissues, one could write:

$$\left|S_{Ratio}^{att}(T) - S_{Ratio}(T)\right| \le \left|L\frac{d[\mu(\lambda_1,T,L)-\mu(\lambda_2,T,L)]}{dT}\right| \quad (4)$$

Expression (4) states that the stronger the thermal dependence of μ_{att}^{eff} at a certain wavelength, the higher the difference between the relative thermal sensitivities obtained in the presence and absence of the tissue. When dealing with ratiometric thermal sensitivities, however, expression (5) indicates that the critical parameter is the difference between the thermal derivatives of μ_{att}^{eff} as measured at the two wavelengths selected to compute the intensity ratio. This, in turns, might explain the reason for the smaller differences in S_{Ratio} when compared to S_{Int} obtained for Ag$_2$S dots (**Figure 5b** and **c**). In addition, it also shows the rational of developing reliable ratiometric LNTh by selecting two wavelengths with similar thermal dependences of the effective attenuation coefficient, so that $\frac{d[\mu(\lambda_1,T,L)-\mu(\lambda_2,T,L)]}{dT} = 0$. Therefore, the determination of spectral regions with equivalent $d\mu(\lambda_c,T,L)/dT$ should be a matter of concern in future studies. At this point, it is worth mentioning that the limits in $S_{\lambda max}$ cannot be explicitly stated in inequalities due to the strong dependence of λ_{max} on the original shape of the spectrum. Nevertheless, if certain assumptions are made (see Section S4 of Supporting Information), similar inequalities may be obtained.

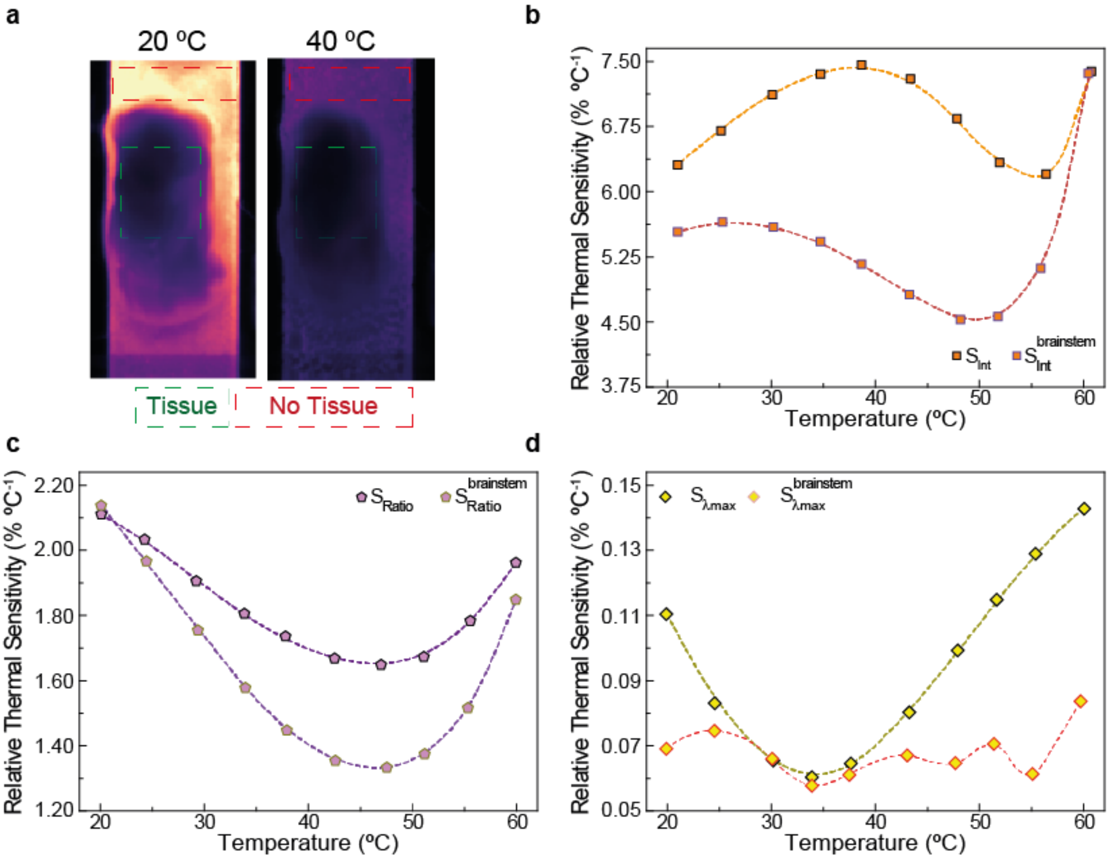

Figure 5. Tissue-induced changes in relative thermal sensitivity. a) Narrowband luminescence images (centered at 1200 nm) of a cuvette containing Ag$_2$S dots when having brainstem on its surface at 20 °C (top) and 40 °C (bottom). Comparison between the relative thermal sensitivity as measured in the presence and absence of tissue for **b)** absolute intensity, **c)** intensity ratio and **d)** peak position. Dashed lines were included as smoothed guide for the eyes.

The impact on subtissue thermal sensing of the reported changes in the thermal sensitivity are here evaluated by a simple experiment. In it, a slice of brainstem (2mm of thickness) was put on the surface of a micro-chamber containing a solution of Ag_2S dots and was then subjected to a heating cycle (see Experimental Section). By using the three thermometric parameters (*Int*, *Ratio* and λ^{max}), one could then dynamically compare the differences produced in the estimation of ΔT by the different calibrations curves of **Figure 5**. A thermographic camera was also utilized for means of comparison. Thermal transients included in **Figure 6a** were obtained by using the calibration curve of Ag_2S dots in the absence of any tissue, whereas **Figure 6b** considers the calibration in the presence of brainstem. Several differences are perceived when comparing them. The first is that, independently of the thermometric parameter selected, $\Delta T(t)$ is always higher in **Figure 6b**. The second difference to notice is that the thermal transients contained in **Figure 6b** are much closer to the one recorded by the thermographic camera. This, in turns, could indicate a better accuracy in temperature estimation. In fact, such a proximity with the surface temperature is predicted by numerical models accounting for laser-induced heat in tissues (see Section S6 of Supporting Information). The greater reliability of the data in **Figure 6b** is further supported by the smaller disagreement between the estimations of $\Delta T(t)$ via different thermometric parameters (*Int*, *Ratio* and λ^{max}). While **Figure 6a** presents temperature discrepancies in ΔT as large as 11 °C, these discrepancies are reduced to 6 °C in **Figure 6b**. The benefits of using the calibration curves obtained in the presence of a tissue are further evidenced in **Figure 6c**, where the average temperatures estimated with the correct, $\langle T\rangle^{correct} = (T_{Int}^{correct} + T_{Ratio}^{correct} + T_{\lambda}^{correct})/3$, and incorrect calibrations, $\langle T\rangle^{incorrect} = (T_{Int}^{incorrect} + T_{Ratio}^{incorrect} + T_{\lambda}^{incorrect})/3$, were computed and their respective standard deviations were plotted as error bars. Though these averages were calculated considering equal weights of reliability for each thermometric parameter, future studies on their relationship with the intrinsic experimental errors may point to a different direction. Nonetheless, the similarity between the shape of the thermographic heating profile and the ones obtained with the correct calibrations, even if not optimally calculated, is uncanny.

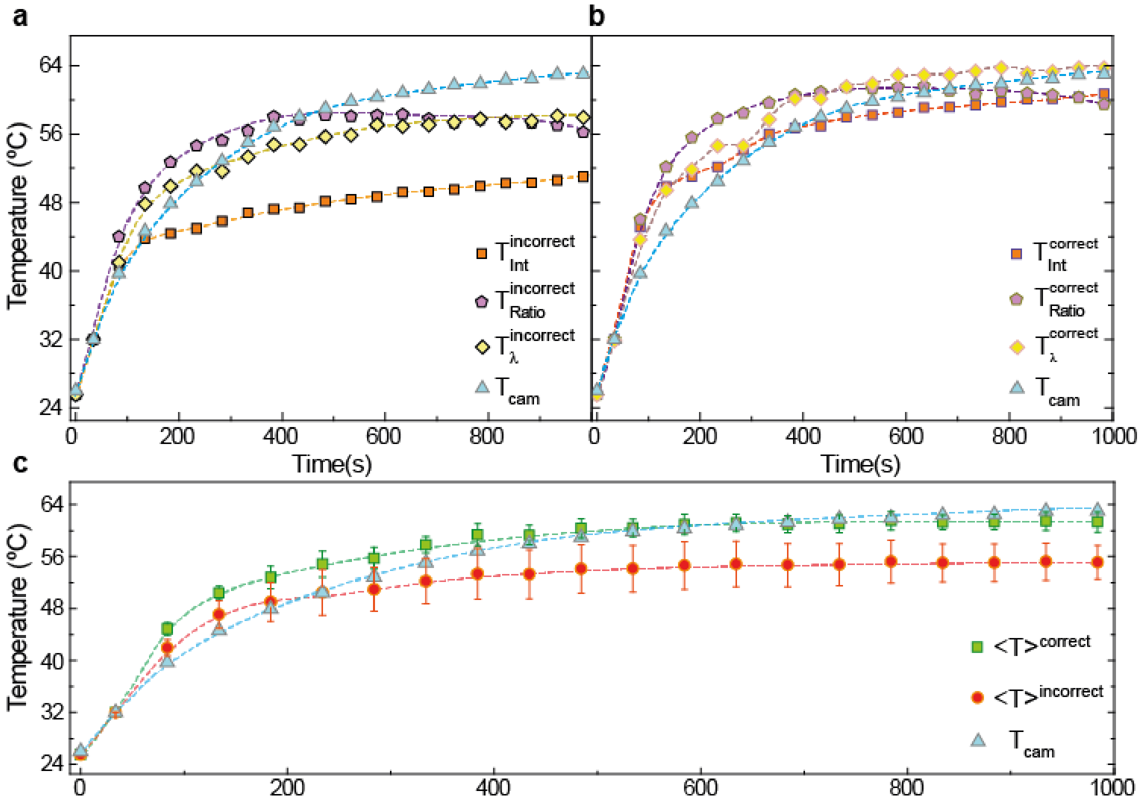

Figure 6. Tissue-induced changes in relative thermal sensitivity. Estimation of ∆T by different thermometric parameters when considering the calibration **a)** with and **b)** without tissues. **c)** Average temperature of the tissue as estimated according to the different calibrations (correct when considering the tissue, incorrect otherwise). Dashed lines were included as smoothed guide for the eyes.

CONCLUSIONS

Hyperspectral *in vivo* imaging is here employed to investigate the role played by the tissue optical properties in *in vivo* luminescence thermometry. This work demonstrates that biological tissues, under various conditions, significantly distort the shape of the spectra of infrared luminescent probes operating within the biological windows. These distortions, in turns, could lead to erroneous thermal readouts. Results here reported also demonstrate how the presence of tissues lead to relevant changes in the calibration curves of luminescent nanothermometers and to thermal sensitivities significantly different from those obtained from aqueous solutions (traditionally used to estimate subtissue temperatures). All these effects are explained by considering the thermal dependence of light absorption and scattering processes in tissues. Simple experiments reveal that the contribution given by the effective attenuation coefficient to the relative thermal sensitivity of luminescent nanothermometers strongly depend on the selected thermometric parameter. Though absolute emission intensity seemed to be the most affected one, the study of a heating transient in a tissue indicated that the changes in other parameters should not be so easily dismissed. In particular we demonstrate how ratiometric thermal sensing, considering as the most reliable approach for remote thermal sensing, is also significantly affected by tissue-induced optical distortions.

This work demonstrates that *in vivo* luminescence nanothermometry is not as reliable as previously thought. It not only constitutes a critical study on the field but it also proposes different ways of avoiding the negative impact that tissue-induced optical distortions have on the accurate determination of subtissue temperature. Based on the results here included, future works dealing with *in vivo* luminescence thermometry should include different quality checks to ensure that the presence of the tissue is not leading to erroneous thermal readouts.

EXPERIMENTAL SECTION

Calibration measurements

When measuring the temperature calibrations, the system under study was put above a thermoelectrically Peltier plate cooled by a refrigerated circulating water bath (MX07R-20-A1 Heidolph) while being imaged by the equipment in **Figure 1**. Its temperature was then varied in the 20 ºC -60 ºC range, with a step of 5 ºC, and 10 different HSI cubes were obtained. A delay of 5 minutes between each measurement had to be considered for the achievement of thermal equilibrium.

Animal experiments

The *in vivo* experiments carried out in this work were approved by the Ethics Committee from Universidad Autónoma de Madrid (CEI) and complied with the principles of good laboratory animal care following the European Directive for the Protection of Animals Used for Scientific Purposes. Two CD1 female mice (weight, 27 g; age, 8 weeks) were used. For the subcutaneous injection, 100 µL of an aqueous dispersion of NPs was used. A 25 gauge sterile needle was inserted to a depth of 1 cm under the pocket made by gently pulling up the skin over the flank. The injection depth was estimated to be 2 mm.The concentrations were 0.15 mg mL^{-1} for Ag_2S dots and 1.5 mg mL^{-1} for Yb@Nd LaF_3 NPs or Er-Yb@Yb-Tm LaF_3 NPs. Intravenous injection of Ag_2S dots (0.15 mg mL^{-1}) was performed using the technique of retro-orbital injection with a 26-G insulin needle and syringe to deliver the NPs in the anesthetized mouse. Isoflurane was used as inhalant anesthetic (4% induction, 1% maintenance), and the *in vivo images* were obtained with the anesthetized animal. After the experiments, euthanasia was performed under isoflurane.

Ex vivo transient thermometry

The measurement of the *ex vivo* thermal transient was performed under the follow conditions: the whole system (brainstem+micro-chamber) was put in the imaging system of **Figure 1** and excited by an 808 nm laser with high intensity (220 mW/cm^2) in such a way that its temperature would follow a heating transient. The subtissue temperature was estimated by the luminescence spectra of the luminescent nanoparticles. In the analysis, the initial temperature of the tissue was considered to be equal to the one initially measured by a thermographic camera (FLIR E40bx) that was coupled to the experimental setup, *i.e.* ≈ 25 °C (see Section S5 of Supportion Information).

Acknowledgements

This work was supported by the Spanish Ministry of Economy and Competitiveness under projects MAT2016-75362-C3-1-R, MAT2017-83111R, and MAT2017-85617-R, by the Instituto de Salud Carlos III (PI16/00812), by the Comunidad Autónoma de Madrid (B2017/BMD-3867RENIMCM), and co-financed by the European Structural and investment fond. Additional funding was provided by the European Commission, Horizon 2020 project NanoTBTech, the Fundación para la Investigación Biomédica del Hospital Universitario Ramón y Cajal project IMP18_38 (2018/0265) and also by COST action CM1403. Y. L. S. acknowledges a scholarship from the China Scholarship Council (No. 201806870023).

References

1. Diederich, C. J. Thermal ablation and high-temperature thermal therapy: Overview of technology and clinical implementation. *International Journal of Hyperthermia* **21**, 745–753 (2005).
2. Toutouzas, K. *et al.* Inflammation in lone atrial fibrillation: New insights by coronary sinus thermography. *International Journal of Cardiology* **134**, 345–350 (2009).
3. Collins, A. J., Ring, E. F., Cosh, J. A. & Bacon, P. A. Quantitation of thermography in arthritis using multi-isothermal analysis. I. The thermographic index. *Annals of the Rheumatic Diseases* **33**, 113–115 (1974).
4. Ng, E. Y.-K. A review of thermography as promising non-invasive detection modality for breast tumor. *International Journal of Thermal Sciences* **48**, 849–859 (2009).
5. Marin, R. *et al.* Heat Conversion: Highly Efficient Copper Sulfide-Based Near-Infrared Photothermal Agents: Exploring the Limits of Macroscopic Heat Conversion (Small 49/2018). *Small* **14**, 1870238 (2018).

6. Brites, C. D. S. *et al.* Thermometry at the nanoscale. *Nanoscale* **4**, 4799 (2012).
7. Wang, X., Wolfbeis, O. S. & Meier, R. J. Luminescent probes and sensors for temperature. *Chem. Soc. Rev.* **42**, 7834 (2013).
8. Brites, C. D. S., Balabhadra, S. & Carlos, L. D. Lanthanide-Based Thermometers: At the Cutting-Edge of Luminescence Thermometry. *Advanced Optical Materials* **7**, 1801239 (2019).
9. Tzeng, Y.-K. *et al.* Time-Resolved Luminescence Nanothermometry with Nitrogen-Vacancy Centers in Nanodiamonds. *Nano Lett.* **15**, 3945–3952 (2015).
10. Bastos, A. R. N. *et al.* Thermal Properties of Lipid Bilayers Determined Using Upconversion Nanothermometry. *Adv. Funct. Mater.* 1905474 (2019) doi:10.1002/adfm.201905474.
11. Kundu, S., Mukherjee, D., Maiti, T. K. & Sarkar, N. Highly Luminescent Thermoresponsive Green Emitting Gold Nanoclusters for Intracellular Nanothermometry and Cellular Imaging: A Dual Function Optical Probe. *ACS Appl. Bio Mater.* **2**, 2078–2091 (2019).
12. Liu, J. *et al.* Visible and Near-Infrared, Multiparametric, Ultrasensitive Nanothermometer Based on Dual-Emission Colloidal Quantum Dots. *ACS Photonics* **6**, 2479–2486 (2019).
13. Marin, R. *et al.* Mercaptosilane-Passivated CuInS $_2$ Quantum Dots for Luminescence Thermometry and Luminescent Labels. *ACS Appl. Nano Mater.* **2**, 2426–2436 (2019).
14. Marciniak, L. *et al.* Enhancing the sensitivity of a Nd 3+ ,Yb 3+ :YVO4 nanocrystalline luminescent thermometer by host sensitization. *Phys. Chem. Chem. Phys.* **21**, 10532–10539 (2019).
15. Wu, S., Min, H., Shi, W. & Cheng, P. Multicenter Metal-Organic Framework-Based Ratiometric Fluorescent Sensors. *Adv. Mater.* 1805871 (2019) doi:10.1002/adma.201805871.
16. Ji, Z. *et al.* Heating-induced abnormal increase in Yb3+ excited state lifetime and its potential application in lifetime luminescence nanothermometry. *Inorg. Chem. Front.* **6**, 110–116 (2019).

17. Gschwend, P. M., Starsich, F. H. L., Keitel, R. C. & Pratsinis, S. E. Nd 3+-Doped BiVO4 luminescent nanothermometers of high sensitivity. *Chem. Commun.* **55**, 7147–7150 (2019).
18. Skripka, A., Morinvil, A., Matulionyte, M., Cheng, T. & Vetrone, F. Advancing neodymium single-band nanothermometry. *Nanoscale* **11**, 11322–11330 (2019).
19. Geitenbeek, R. G. *et al.* In Situ Luminescence Thermometry To Locally Measure Temperature Gradients during Catalytic Reactions. *ACS Catal.* **8**, 2397–2401 (2018).
20. Wylezich, T. *et al.* One Ion, Many Facets: Efficient, Structurally and Thermally Sensitive Luminescence of Eu2+ in Binary and Ternary Strontium Borohydride Chlorides. *Chem. Mater.* acs.chemmater.9b03048 (2019) doi:10.1021/acs.chemmater.9b03048.
21. Albers, A. E. *et al.* Dual-Emitting Quantum Dot/Quantum Rod-Based Nanothermometers with Enhanced Response and Sensitivity in Live Cells. *J. Am. Chem. Soc.* **134**, 9565–9568 (2012).
22. Dong, B. *et al.* Temperature Sensing and In Vivo Imaging by Molybdenum Sensitized Visible Upconversion Luminescence of Rare-Earth Oxides. *Adv. Mater.* **24**, 1987–1993 (2012).
23. Yang, Y. *et al.* Fluorescent N-Doped Carbon Dots as *in Vitro* and *in Vivo* Nanothermometer. *ACS Appl. Mater. Interfaces* **7**, 27324–27330 (2015).
24. Haro-González, P. *et al.* Quantum Dot-Based Thermal Spectroscopy and Imaging of Optically Trapped Microspheres and Single Cells. *Small* **9**, 2162–2170 (2013).
25. Cui, Y. *et al.* Dual-Emitting MOF⊃Dye Composite for Ratiometric Temperature Sensing. *Adv. Mater.* **27**, 1420–1425 (2015).
26. Shang, L., Stockmar, F., Azadfar, N. & Nienhaus, G. U. Intracellular Thermometry by Using Fluorescent Gold Nanoclusters. *Angew. Chem. Int. Ed.* **52**, 11154–11157 (2013).
27. Cui, Y., Zhu, F., Chen, B. & Qian, G. Metal–organic frameworks for luminescence thermometry. *Chem. Commun.* **51**, 7420–7431 (2015).

28. McLaurin, E. J., Bradshaw, L. R. & Gamelin, D. R. Dual-Emitting Nanoscale Temperature Sensors. *Chem. Mater.* **25**, 1283–1292 (2013).

29. McLaurin, E. J., Vlaskin, V. A. & Gamelin, D. R. Water-Soluble Dual-Emitting Nanocrystals for Ratiometric Optical Thermometry. *J. Am. Chem. Soc.* **133**, 14978–14980 (2011).

30. Saccomandi, P., Schena, E. & Silvestri, S. Techniques for temperature monitoring during laser-induced thermotherapy: An overview. *International Journal of Hyperthermia* **29**, 609–619 (2013).

31. Cerón, E. N. *et al.* Hybrid Nanostructures for High-Sensitivity Luminescence Nanothermometry in the Second Biological Window. *Adv. Mater.* **27**, 4781–4787 (2015).

32. Rocha, U. *et al.* Subtissue Thermal Sensing Based on Neodymium-Doped LaF_3 Nanoparticles. *ACS Nano* **7**, 1188–1199 (2013).

33. Marciniak, L., Prorok, K., Francés-Soriano, L., Pérez-Prieto, J. & Bednarkiewicz, A. A broadening temperature sensitivity range with a core–shell YbEr@YbNd double ratiometric optical nanothermometer. *Nanoscale* **8**, 5037–5042 (2016).

34. Yang, F. *et al.* An Integrated Multifunctional Nanoplatform for Deep-Tissue Dual-Mode Imaging. *Adv. Funct. Mater.* **28**, 1706235 (2018).

35. Weissleder, R. A clearer vision for in vivo imaging. *Nat Biotechnol* **19**, 316–317 (2001).

36. Bashkatov, A. N., Genina, E. A., Kochubey, V. I. & Tuchin, V. V. Optical properties of human skin, subcutaneous and mucous tissues in the wavelength range from 400 to 2000 nm. *J. Phys. D: Appl. Phys.* **38**, 2543–2555 (2005).

37. Wang, F. *et al.* Light-sheet microscopy in the near-infrared II window. *Nat Methods* **16**, 545–552 (2019).

38. Wan, H. *et al.* A bright organic NIR-II nanofluorophore for three-dimensional imaging into biological tissues. *Nat Commun* **9**, 1171 (2018).

39. Hong, G., Antaris, A. L. & Dai, H. Near-infrared fluorophores for biomedical imaging. *Nat Biomed Eng* **1**, 0010 (2017).

40. Zhu, S. *et al.* 3D NIR-II Molecular Imaging Distinguishes Targeted Organs with High-Performance NIR-II Bioconjugates. *Adv. Mater.* **30**, 1705799 (2018).

41. Carvajal Marti, J. J. *et al.* Expanding luminescence thermometry detection range to the SWIR for biomedical applications. in *Optical Sensing and Detection V* (eds. Berghmans, F. & Mignani, A. G.) 34 (SPIE, 2018). doi:10.1117/12.2306418.

42. Kamimura, M., Matsumoto, T., Suyari, S., Umezawa, M. & Soga, K. Ratiometric near-infrared fluorescence nanothermometry in the OTN-NIR (NIR II/III) biological window based on rare-earth doped β-NaYF $_4$ nanoparticles. *J. Mater. Chem. B* **5**, 1917–1925 (2017).

43. Sekiyama, S. *et al.* Temperature Sensing of Deep Abdominal Region in Mice by Using Over-1000 nm Near-Infrared Luminescence of Rare-Earth-Doped NaYF4 Nanothermometer. *Sci Rep* **8**, 16979 (2018).

44. Ximendes, E. C. *et al.* Unveiling in Vivo Subcutaneous Thermal Dynamics by Infrared Luminescent Nanothermometers. *Nano Lett.* **16**, 1695–1703 (2016).

45. Ximendes, E. C. *et al.* In Vivo Subcutaneous Thermal Video Recording by Supersensitive Infrared Nanothermometers. *Adv. Funct. Mater.* **27**, 1702249 (2017).

46. Santos, H. D. A. *et al.* In Vivo Early Tumor Detection and Diagnosis by Infrared Luminescence Transient Nanothermometry. *Adv. Funct. Mater.* **28**, 1803924 (2018).

47. Ximendes, E. C. *et al.* In Vivo Ischemia Detection by Luminescent Nanothermometers. *Adv. Healthcare Mater.* **6**, 1601195 (2017).

48. del Rosal, B., Ximendes, E., Rocha, U. & Jaque, D. In Vivo Luminescence Nanothermometry: from Materials to Applications. *Advanced Optical Materials* **5**, 1600508 (2017).

49. Labrador-Páez, L. *et al.* Reliability of rare-earth-doped infrared luminescent nanothermometers. *Nanoscale* **10**, 22319–22328 (2018).

50. Crawford, A. C., Skuratovsky, A. & Porter, M. D. Sampling Error: Impact on the Quantitative Analysis of Nanoparticle-Based Surface-Enhanced Raman Scattering Immunoassays. *Anal. Chem.* **88**, 6515–6522 (2016).

51. Boyd, R. D., Pichaimuthu, S. K. & Cuenat, A. New approach to inter-technique comparisons for nanoparticle size measurements; using atomic force microscopy, nanoparticle tracking analysis and dynamic light scattering. *Colloids and Surfaces A: Physicochemical and Engineering Aspects* **387**, 35–42 (2011).
52. Garcia, M. A. *et al.* Sources of experimental errors in the observation of nanoscale magnetism. *Journal of Applied Physics* **105**, 013925 (2009).
53. Grandke, J., Resch-Genger, U., Bremser, W., Garbe, L.-A. & Schneider, R. J. Quality assurance in immunoassay performance-temperature effects. *Anal. Methods* **4**, 901 (2012).
54. Wang, S.-Y., Huang, S. & Borca-Tasciuc, D.-A. Potential Sources of Errors in Measuring and Evaluating the Specific Loss Power of Magnetic Nanoparticles in an Alternating Magnetic Field. *IEEE Trans. Magn.* **49**, 255–262 (2013).
55. Gaufrès, E. *et al.* Hyperspectral Raman imaging using Bragg tunable filters of graphene and other low-dimensional materials: Hyperspectral Raman imaging using Bragg tunable filters of graphene and other low-dimensional materials. *J. Raman Spectrosc.* **49**, 174–182 (2018).
56. Mishra, P. *et al.* Close range hyperspectral imaging of plants: A review. *Biosystems Engineering* **164**, 49–67 (2017).
57. Amigo, J. M., Babamoradi, H. & Elcoroaristizabal, S. Hyperspectral image analysis. A tutorial. *Analytica Chimica Acta* **896**, 34–51 (2015).
58. Bock, C. H., Parker, P. E., Cook, A. Z. & Gottwald, T. R. Visual Rating and the Use of Image Analysis for Assessing Different Symptoms of Citrus Canker on Grapefruit Leaves. *Plant Disease* **92**, 530–541 (2008).
59. Galassi, T. V. *et al.* An optical nanoreporter of endolysosomal lipid accumulation reveals enduring effects of diet on hepatic macrophages in vivo. *Sci. Transl. Med.* **10**, eaar2680 (2018).

60. Star, W. M., Marijnissen, J. P. A. & Gemert, M. J. C. van. Light dosimetry in optical phantoms and in tissues: I. Multiple flux and transport theory. *Phys. Med. Biol.* **33**, 437–454 (1988).
61. Sordillo, L. A., Pu, Y., Pratavieira, S., Budansky, Y. & Alfano, R. R. Deep optical imaging of tissue using the second and third near-infrared spectral windows. *J. Biomed. Opt* **19**, 056004 (2014).
62. Gendrin, C., Roggo, Y. & Collet, C. Pharmaceutical applications of vibrational chemical imaging and chemometrics: A review. *Journal of Pharmaceutical and Biomedical Analysis* **48**, 533–553 (2008).
63. Gowen, A. A., Feng, Y., Gaston, E. & Valdramidis, V. Recent applications of hyperspectral imaging in microbiology. *Talanta* **137**, 43–54 (2015).
64. Mishra, P. *et al.* Detection and Quantification of Peanut Traces in Wheat Flour by near Infrared Hyperspectral Imaging Spectroscopy Using Principal-Component Analysis. *Journal of Near Infrared Spectroscopy* **23**, 15–22 (2015).
65. Mishra, P. *et al.* Application of independent components analysis with the JADE algorithm and NIR hyperspectral imaging for revealing food adulteration. *Journal of Food Engineering* **168**, 7–15 (2016).
66. Matsuda, O., Tanaka, A., Fujita, T. & Iba, K. Hyperspectral Imaging Techniques for Rapid Identification of Arabidopsis Mutants with Altered Leaf Pigment Status. *Plant and Cell Physiology* **53**, 1154–1170 (2012).
67. Yakovliev, A. *et al.* Hyperspectral Multiplexed Biological Imaging of Nanoprobes Emitting in the Short-Wave Infrared Region. *Nanoscale Res Lett* **14**, 243 (2019).
68. Gowen, A., Odonnell, C., Cullen, P., Downey, G. & Frias, J. Hyperspectral imaging – an emerging process analytical tool for food quality and safety control. *Trends in Food Science & Technology* **18**, 590–598 (2007).

69. Bhatt, M., Ayyalasomayajula, K. R. & Yalavarthy, P. K. Generalized Beer–Lambert model for near-infrared light propagation in thick biological tissues. *J. Biomed. Opt* **21**, 076012 (2016).
70. Sassaroli, A. & Fantini, S. Comment on the modified Beer–Lambert law for scattering media. *Phys. Med. Biol.* **49**, N255–N257 (2004).
71. Kocsis, L., Herman, P. & Eke, A. The modified Beer–Lambert law revisited. *Phys. Med. Biol.* **51**, N91–N98 (2006).
72. Son, I.-Y. & Yazici, B. Near infrared imaging and spectroscopy for brain activity monitoring. in *Advances in Sensing with Security Applications* (eds. Byrnes, J. & Ostheimer, G.) vol. 2 341–372 (Kluwer Academic Publishers, 2006).
73. Marciniak, Ł. *et al.* Near infrared absorbing near infrared emitting highly-sensitive luminescent nanothermometer based on Nd $^{3+}$ to Yb $^{3+}$ energy transfer. *Phys. Chem. Chem. Phys.* **17**, 24315–24321 (2015).
74. Ogle, M. M. *et al.* Sensing Temperature in Vitro and in Cells Using a BODIPY Molecular Probe. *J. Phys. Chem. B* **123**, 7282–7289 (2019).
75. Doughty, A. *et al.* Nanomaterial Applications in Photothermal Therapy for Cancer. *Materials* **12**, 779 (2019).
76. van der Meer, F. J., Faber, D. J., Çilesiz, I., van Gemert, M. J. C. & van Leeuwen, T. G. Temperature-dependent optical properties of individual vascular wall components measured by optical coherence tomography. *J. Biomed. Opt.* **11**, 041120 (2006).
77. Su, Y. *et al.* Measurements of the thermal coefficient of optical attenuation at different depth regions of in vivo human skins using optical coherence tomography: a pilot study. *Biomed. Opt. Express* **6**, 500 (2015).
78. Laufer, J., Simpson, R., Kohl, M., Essenpreis, M. & Cope, M. Effect of temperature on the optical properties of ex vivo human dermis and subdermis. *Phys. Med. Biol.* **43**, 2479–2489 (1998).

79. Vogt, W. C., Barton, J. K., Agrawal, A. & Pfefer, T. J. Measurement and Thermal Dependence of Biological Tissue Optical Properties. in *Theory and Applications of Heat Transfer in Humans* (ed. Shrivastava, D.) 355–378 (John Wiley & Sons Ltd, 2018). doi:10.1002/9781119127420.ch18.

80. Pettit, G. H., Ediger, M. N. & Weiblinger, R. P. Dynamic optical properties of collagen-based tissue during ArF excimer laser ablation. *Appl. Opt.* **32**, 488 (1993).

81. Çilesiz, I. F. & Welch, A. J. Light dosimetry: effects of dehydration and thermal damage on the optical properties of the human aorta. *Appl. Opt.* **32**, 477 (1993).

82. Pickering, J. W. *et al.* Changes in the optical properties (at 6328 nm) of slowly heated myocardium. *Appl. Opt.* **32**, 367 (1993).

83. Nilsson, A. M. K., Lucassen, G. W., Verkruysse, W., Andersson-Engels, S. & van Gemert, M. J. C. Changes in Optical Properties of Human Whole Blood *in vitro* Due to Slow Heating. *Photochemistry and Photobiology* **65**, 366–373 (1997).

84. Jerath, M. R., Gardner, C. M., Rylander, H. G. & Welch, A. J. Dynamic optical property changes: Implications for reflectance feedback control of photocoagulation. *Journal of Photochemistry and Photobiology B: Biology* **16**, 113–126 (1992).